Research Article

ADVANCED PHOTONICS

In situ photoelectric biosensing based on ultranarrowband near-infrared plasmonic hot electron photodetection

Xianghong Nan,[a,†] Wenduo Lai,[a,†] Jie Peng,[b] Haiquan Wang,[a] Bojun Chen,[a] Huifan He,[a] Zekang Mo,[a] Zikun Xia,[a] Ning Tan,[a] Zhong Liu,[c] Long Wen,[a,*] Dan Gao,[b] and Qin Chen[a,*]

[a]Jinan University, College of Physics & Optoelectronic Engineering, Institute of Nanophotonics, Guangdong Provincial Key Laboratory of Nanophotonic Manipulation, Guangzhou, China

[b]Tsinghua University, Shenzhen International Graduate School, State Key Laboratory of Chemical Oncogenomics, Shenzhen, China

[c]Jinan University, College of Life Science and Technology, Guangzhou, China

Abstract. Narrowband photodetection is an important measurement technique for material analysis and sensing, for example, nondispersive infrared sensing technique. Both photoactive material engineering and nanophotonic filtering schemes have been explored to realize wavelength-selective photodetection, while most devices have a responsive bandwidth larger than 2% of the operating wavelength, limiting sensing performance. Near-infrared photodetection with a bandwidth of less than 0.2% of the operating wavelength was demonstrated experimentally in Au/Si Schottky nanojunctions. A minimum linewidth of photoelectric response down to 2.6 nm was obtained at a wavelength of 1550 nm by carefully tailing the absorptive and radiative loss in the nanostructures. Multiple functions were achieved on chip with the corrugated Au film, including narrowband resonance, light harvesting for sensing and photodetection, and electrodes for hot electron emission. Benefiting from such a unity integration with *in situ* photoelectric conversion of the optical sensing signal and the ultranarrowband resonance, self-contained on-chip biosensing via simple intensity interrogation was demonstrated with a limit of detection down to 0.0047% in concentration for glucose solution and 150 ng/mL for rabbit IgG. Promising potential of this technique is expected for the applications in on-site sensing, spectroscopy, spectral imaging, etc.

Keywords: plasmonics; hot electron; sensor; photodetector; spectroscopy.

Received Sep. 30, 2023; revised manuscript received Jan. 4, 2024; accepted for publication Mar. 4, 2024; published online Mar. 22, 2024.

[DOI: 10.1117/1.AP.6.2.026007]

1 Introduction

Wavelength-selective photodetection has been widely applied in nondispersive infrared sensing, biofluorescent imaging, spectral imaging, optics communication, surveillance, and machine vision,[1–5] where only a small spectral range of light around a central wavelength (λ_0) needs to be detected while the remainder should be excluded. In general, photodetectors (PDs) are broadband with a photoresponsive bandwidth determined by the onset (λ_{on}) and the switch-off (λ_{off}) wavelengths associated with material properties. Narrowband photodetection is usually realized by two types of approaches. (1) Engineering photoactive materials and detector structures for independent control over λ_{on} and λ_{off}, such as dye blending,[6] charge collection narrowing,[7,8] carrier trapping,[9] self-trapped state,[10] depletion region engineering,[11] and gate transmittance tuning.[12] (2) Combining broadband PDs with narrowband filters, such as resonant cavities (RCs),[13,14] nanodisk arrays,[15] photonic crystals,[16] metamaterials,[17] nanowires,[18] epsilon-near-zero effect,[19,20] and surface plasmon resonance (SPR).[21–23] In some cases, the components for photodetection and spectral filtering are actually merged into a single device structure.[23] As shown in Table S1 in the Supplementary

*Address all correspondence to Long Wen, longwen@jnu.edu.cn; Qin Chen, chenqin2018@jnu.edu.cn

†These authors contributed equally to this work.

Material, the reported full width at half-maximum (FWHM) of narrowband PDs developed by engineering photoactive material and device structure is between 10 and 110 nm. For the former, a minimum of the normalized response bandwidth (FWHM/λ_0) of 2.6% is observed in a self-trapped state enabled filterless narrowband PD in two-dimensional layered perovskite single crystals.[10] For the latter, the photoelectric responses of most PDs also cover a relatively broad band over 10 nm except the RC PDs, where strong optical resonance via 40 pairs of bottom GaAs/AlAs distributed Bragg reflector (DBR) mirrors and three pairs of top ZnSe/GaF_2 DBR mirrors contribute to an FWHM of 4 nm.[13] Although microring/microdisk filters with ultrahigh quality (Q) factors can be integrated with waveguide PDs to realize narrowband photodetection,[24–26] scaling up the spectral channel meets with significant difficulties due to waveguide coupling and interconnection. In contrast, vertical incidence devices (e.g., focal plane array with millions of pixels) are preferred in high throughput biosensing, spectral imaging, etc. So far, only the RC PD is applicable for spectrally selective photodetection in a vertical incidence configuration with a high spectral accuracy (FWHM/$\lambda_0 < 1\%$). However, the several tens of pairs of DBR mirrors significantly increase the processing complexity in the device fabrication. The cavity thickness-dependent wavelength tuning mechanism is also limited in its applications due to the complex fabrication process of a filter array.

In this paper, near-infrared (NIR) photodetection with a normalized response bandwidth FWHM/λ_0 of 0.17% was demonstrated experimentally in Au/Si Schottky nanojunctions. Due to the low-loss plasmonic resonance supported by Au-covered shallow silicon gratings, the linewidth was reduced to 1/20 of the conventional prism-coupled SPR supported by a planar Au film on quartz. Grating height, light-source divergence, and linewidth were manipulated to push the limit of the measured photodetection bandwidth down to 2.6 nm at a wavelength of 1550 nm. Benefiting from the narrowband resonance and the strongly localized SPR field, a refractive index detection limit down to 2.5×10^{-6} RIU was achieved. Furthermore, self-contained on-chip optical sensing was realized with *in situ* hot electron (HE)-based photoelectric conversion in such a metal-semiconductor (MS) nanojunction. Bio/chemo sensing on both glucose and goat IgG solutions was conducted, demonstrating excellent sensing performance comparable to bulky commercial biosensing instruments.

2 Materials and Methods

2.1 Optical Simulation

Absorption spectra and electromagnetic field distribution were simulated by using the finite-difference time-domain method. The structure parameters are given in the figure legends. Periodic boundary conditions were applied in the grating plane and perfectly matched layer boundary conditions were applied in the direction along light transmission. Polarization was set to be perpendicular to the grating direction.

2.2 Device Fabrication

Nanogratings in a layer of 500 nm thick photoresist (Shipley 1805) were first patterned on a 10 cm n-Si wafer (1–10 Ω cm) using a Nikon NSR i-line stepper. A dry etching process was adopted to transfer the patterns into Si with reactive ion etching (RIE, Tegal 903e). A stack of 10 nm Al_2O_3 and 200 nm SiO_2 was deposited outside the grating region (3 mm × 3 mm) as an insulator layer for electrode deposition (15 nm Ti/100 nm Al/15 nm Ti/100 nm Au). In comparison, a stack of 1 nm Ti and 60 nm Au was deposited in the grating region by magnetron sputtering. Successively, Al film (300 nm) was deposited on the entire rear side of a wafer. The whole wafer was cut into small pieces (2 cm × 1.5 cm) and then bonded with the microfluidic channels in PDMS. The complete devices were mounted on printed circuit board and linked electrically by wire bonding.

2.3 Optical and Optoelectrical Measurements

A high-power supercontinuum laser (NKT Photonics) coupled with acousto-optic tunable filters (AOTFs) was employed as a monochromatic and linearly polarized (1:100) light source in optical and optoelectrical measurements. The reflection spectra were collected by scanning the wavelength of this laser source and recording the power of the reflected light by a power meter (Thorlabs PM100D). The near-field mapping experiments were performed by the s-SNOM (Neaspec GmbH). A tunable laser (Santec, TSL-570) with a linewidth of 1 pm is also used for accurate spectral measurement for comparison. All the electrical characteristics, including the $I - V$ curves and the time-resolved currents, were collected using a source meter (Keithley 2636B).

In the glucose and rabbit IgG sensing experiments, solutions with different concentrations were injected to the sensor via the microfluidics. The surface of the Au film of the sensor was functionalized with the goat anti-rabbit IgG. Rabbit IgG solutions with three different concentrations were prepared for biosensing experiments.

3 Results

The proposed narrowband NIR PD, which consists of Au-covered Si gratings, is shown in Fig. 1(a). The corrugated Au film has dual functions, i.e., supporting SPR for spatial/spectral engineering and acting as an electrode for HE emission. On the one hand, a Schottky junction is formed at the Au/Si interface and the ohmic electrode is formed at the back side of the Si substrate. As a result, interband transition in Si dominates the photoelectric response under illumination with a wavelength smaller than 1100 nm, while the photogenerated HEs,[27–33] as shown in Fig. 1(b), become the main contribution factor for the subbandgap photodetection of Si. In previous works, Au/Si Schottky PDs demonstrated a broad operating wavelength range from 400 to 2000 nm.[27–29] On the other hand, wavelength-dependent photodetection is achieved by SPR-modulated light absorption. Although plasmonic antennas, Tamm state, and metasurfaces have been used to tune the photoelectric response,[34–36] spectrally selective photodetection was realized in a relatively broad band down to 30 nm with a normalized response bandwidth well above 3%. Lower detection limits of optical sensing and higher spectral resolutions of spectral imaging can be expected with a smaller linewidth of the photoelectric response.

3.1 Narrowband Plasmonic Resonance

Considering the actual requirements of high yield and low cost in device fabrication, sub-100 nm nanostructures such as nanoantennas and several tens of layers of multilayer stack such as DBRs were not considered in our design. Instead, gratings with a period between 800 and 1200 nm were adopted, which can be

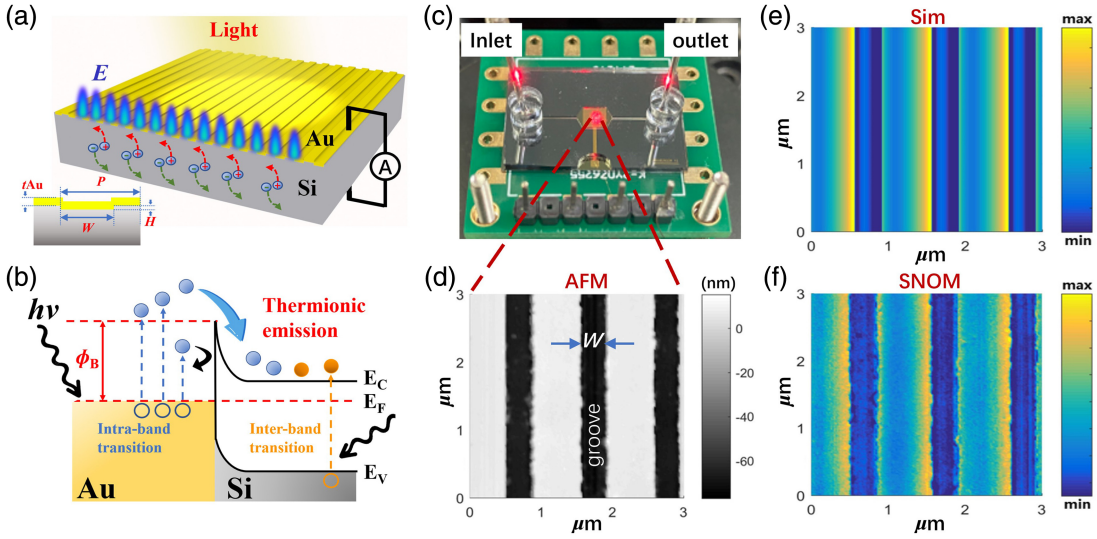

Fig. 1 Au-covered Si gratings used for narrowband NIR photodetection. (a) Schematic of the proposed Au/Si nanojunction. Surface localized plasmonic resonance supported by the Au/Si gratings is plotted with an overlap to the gratings, which is expected to improve the surface sensing. The *in situ* photoelectric conversion concept is also indicated as a unique property in this Au/Si nanojunction platform. (b) Schematic of the energy band structure of the Au/Si Schottky junction indicating two photodetection mechanisms. (c) Photograph of the fabricated PD integrated with microfluidics. (d) An AFM image of the fabricated Au/Si gratings with a period of 1 μm. (e) Numerical simulation of the electrical field distribution at a wavelength of $\lambda = 1550$ nm at an incident angle of 3 deg. Grating period $P = 1000$ nm, width $W = 400$ nm, height $H = 50$ nm, thickness of Au film $t_{Au} = 50$ nm. (f) The s-SNOM mapping results.

patterned in a single lithography step in seconds on a whole 10 cm silicon wafer (see Sec. 2). The gratings couple the on-resonance incident light to SPR supported by the corrugated Au film, forming a strongly localized surface mode, as shown in Fig. 1(a). Each PD has an active region of 3 mm × 3 mm defined by the metallic gratings, and microfluidics were integrated on top of the device for the following sensing experiments, as shown in Fig. 1(c). The three-dimensional profile of Au/Si gratings was measured using AFM, where the sharp contrast at the boundaries indicates the well-controlled lithography and dry-etching processes, as shown in Fig. 1(d). The numerical simulation in Fig. 1(e) clearly shows the surface-confined optical resonance in the near field (see Sec. 2). The maximum field components can be seen around the corners of the gratings, and the asymmetry is caused by the oblique incidence (3 deg) to mimic the experiments in scattering-type scanning near-field optical microscopy (s-SNOM) (see Sec. 2). The results of the SNOM mapping in Fig. 1(f) agree well with the simulation results. The strongly localized field components at the grating surface verified by both simulation and experiment results demonstrate the promising potential to boost the photodetection efficiency (increase light absorption in Au) and further reduce the detection limit of optical sensing (increase the sensitivity to the surface environment).

Narrowband resonance can be clearly seen from the calculated absorption spectra of the Au/Si gratings, as shown in Fig. 2(a), where the resonant wavelength, i.e., the operating wavelength band of the PDs, can be continuously tuned by simply changing the grating period. It is a major advantage over the vertical cavity PD for mass manufacturing, particularly for a PD array with various operating wavelengths. As seen, there is only one absorption peak in a broad band of 800 to 1800 nm with low background and sidelobes due to the continuous Au film, which is important for nondispersive infrared (NDIR) sensing to exclude the interference signal. An FWHM of 6.49 nm is observed with an absorption peak at 922 nm for $P = 900$ nm, i.e., a normalized bandwidth of 0.7%. Because the spectral photoelectric response of this PD is mainly determined by the resonance, it is reasonable to expect similar narrowband photodetection performance, which suggests its promising applications in biosensing and spectral imaging. To evaluate the impact of a resonant linewidth on the sensing performance, a series of normalized Lorentz-type curves with different FWHMs, as shown in Fig. 2(b), were used to mimic the resonance spectra of plasmonic sensing structures. Assuming a same resonance shift of 2 nm, the maximum amplitude change of a resonance with a small linewidth (FWHM = 5 nm) is 28 times that of a resonance with a large linewidth (FWHM = 150 nm), i.e., the detection limit is expected to be reduced by more than 1 order of magnitude by using a narrowband resonance. Therefore, it is important to find out the major factors associated with the resonance linewidth in both design and experiment.

3.2 Dominant Factors of Resonant Linewidth

Using a time-domain coupled mode theory, the guide line for designing a narrow-band resonance can be obtained (Supplementary Material S2). Basically, there are two main loss mechanisms of such one-port resonant configuration. One is the absorption loss associated with the lossy metal; the other is the radiative loss caused by the leaky modes of the gratings. A perfect matching between the absorption loss and the radiative loss

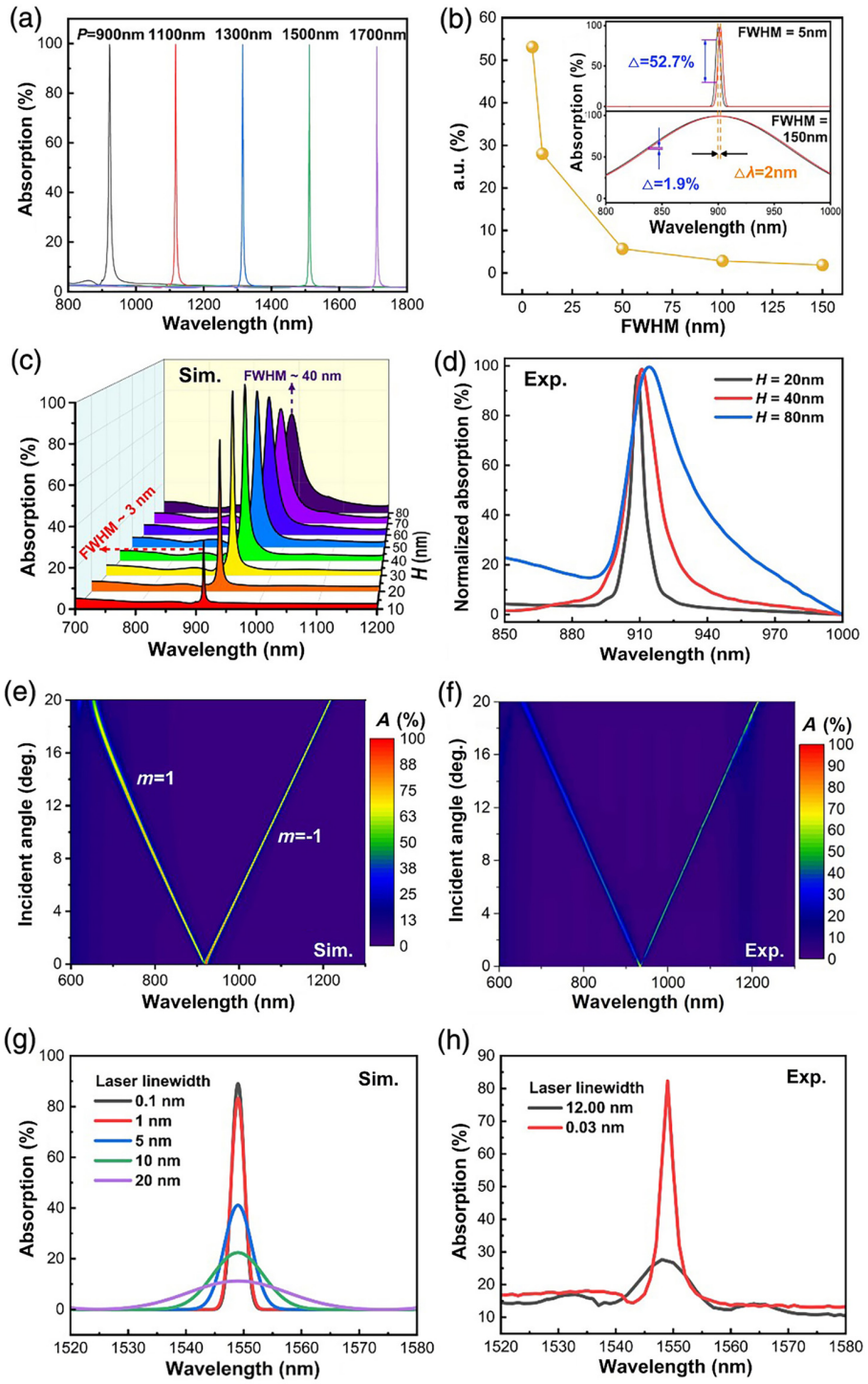

Fig. 2 Optical characterization of Au/Si gratings. (a) Simulated absorption spectra for $P = 900$, 1100, 1300, 1500, and 1700 nm. $H = 28$ nm, $W = 550$ nm, and $t_{Au} = 60$ nm. (b) Maximum amplitude variation of a normalized Lorentz-type on-resonance spectrum with different FWHMs, assuming a same resonance shift of 2 nm. The insets show the cases of FWHM = 5 and 150 nm. (c), (d) Calculated and normalized measured absorption spectra for $H = 20$, 40, and 80 nm. $P = 900$ nm, $W = 500$ nm, and $t_{Au} = 60$ nm. (e), (f) Calculated and measured absorption spectra at different incidence angles. $P = 900$ nm, $H = 28$ nm, $W = 550$ nm, and $t_{Au} = 60$ nm. (g) Calculated absorption spectra mimicking the wavelength-scanning measurement process in the cases of different passband linewidth settings of the AOTF. $P = 900$ nm, $H = 28$ nm, $W = 477$ nm, and $t_{Au} = 60$ nm. The incident angle is 45 deg. (h) Measured absorption spectra with both an NKT supercontinuum laser source (12 nm linewidth) and a Santec tunable laser (0.03 nm linewidth).

leads to unity light absorption at resonance. The radiation loss is mainly determined by the grating height, and thus shallow gratings are required for a narrow linewidth. The absorption loss is less sensitive to the structure dimensions, and it sets the lower limit of the linewidth. As shown in Fig. 2(c), an FWHM of 6.9 nm in calculation is obtained at $H = 30$ nm with a peak absorption of 100%. With the increase of the grating height, the FWHM increases up to 40 nm for $H = 80$ nm. Although an FWHM of 3 nm can be obtained at $H = 10$ nm, the absorption is less than 34%, which is caused by the mismatch of absorption loss and radiative loss. These theoretical and numerical results are verified by the experiment results, as shown in Fig. 2(d), where the normalized absorption spectra were obtained from the measured reflection spectra (no transmission from the back side of the Si). The FWHM monotonically decreases from 31.3 to 5.7 nm when the grating height continuously decreases from 80 to 20 nm. Therefore, shallow gratings fabricated with stable processes are preferred. In addition, by increasing the grating period at a fixed grating height, as shown in Fig. 2(a), the FWHM of the absorption peak keeps decreasing down to 2.65 nm for $P = 1700$ nm with a normalized bandwidth of 0.15%, which is much smaller than the results in the literature (Table S1 in the Supplementary Material). The small FWHM at a large period is determined by the reduced radiative loss due to the small normalized grating height (normalized to the resonance wavelength).

Apart from the impact of structure design and fabrication process, the divergence and the linewidth of the light source were found to be also key factors in determining the measured resonance linewidth. In the experiments, the reflection spectra were measured in a scanning mode using a supercontinuum laser source connected with an AOTF. Due to the grating coupling mechanism in the excitation of SPR in this device, the resonant absorption is sensitive to the incident angle, as shown in Fig. 2(e) (S3 in the Supplementary Material). With an increase of incident angle, a single resonance at normal incidence splits into two resonances, where the one shifting to the longer wavelength is −1st order resonance and the other shifting to the shorter wavelength is +1st order resonance. For an incident angle of 20 deg, the calculated resonant shifts of both −1st and +1st order resonances reach ∼300 nm, which agree well with the experiment results in Fig. 2(f). In a case of divergent incident light, different SPR resonances can be excited at different angles, i.e., the absorption band inevitably extends to a broad wavelength range. In addition, the spectral resolution of the AOTF also limits the minimum measured linewidth. Because the spectral sampling of the plasmonic structures was obtained by continuously tuning the passband of the AOTF, the resonance in the measured spectrum would be broadened if its linewidth is smaller than the width of the passband of the AOTF, which is 10 to 15 nm in NIR. As shown in Fig. 2(g), the width of the AOTF passband was assured in calculation to be 0.1, 1, 5, 10, and 20 nm, respectively, where the simulated absorption spectra mimicking the wavelength-scanning measurement process were obtained by the integration of the filtering response of the AOTF and the absorption spectrum of the Au/Si gratings. Therefore, the calculated results are dependent on the passband linewidth of the AOTF. For a narrowband filtering setting of the AOTF (e.g., 0.1 nm), the calculated linewidth is mainly determined by the linewidth of the absorption spectrum of Si/Au gratings. In contrast, for a broadband filtering setting of the AOTF (e.g., 20 nm), the calculated linewidth is mainly determined by the passband linewidth of the AOTF. In addition, the peak absorption decreases at a broadband filtering setting of the AOTF due to the overall increasing illumination power in a broad band for normalization. This phenomenon was also observed in experiments, as shown in Fig. 2(h), where the black line was measured using a supercontinuum laser source with an AOTF (the FWHM is 10 to 12 nm), and the red line was measured with a tunable laser (Santec, TSL-570) with a linewidth of 200 kHz. Therefore, a narrow linewidth laser source is preferred to maximize the excellent sensing performance in terms of intensity interrogation for sensing.

3.3 Narrowband Plasmonic Photodetection

Based on the above optical measurement, the photoelectric properties of an optimized PD were further characterized, as shown in Fig. 3. The $I - V$ curves under laser light illumination at a wavelength of 1342 nm show a clear Schottky junction behavior, as shown in Fig. 3(a). By continuously switching the wavelength of the laser light illumination by an AOTF, the photocurrent spectrum was recorded, as shown in Fig. 3(b). From 850 to 950 nm, there is only one photocurrent maximum at 914 nm associated with the resonant absorption with low background, which indicates the expected wavelength-selective photodetection. The absorption spectra of this device were obtained from the measured reflection, as shown in Fig. 3(c). The measured resonance wavelength is in an excellent match with the simulation due to the well-controlled grating period in stepper lithography. An absorption peak at 914 nm with an FWHM of 6.44 nm can be seen at normal incidence. The lower peak absorption, slightly larger background, and broader resonance (FWHM = 5 nm in simulation) in experiments were attributed to the measured error [as discussed in Figs. 2(e)–2(h)] and the fabrication errors on the gratings. Compared to the widely used prism-coupled SPR (FWHM = 104.9 nm) in biosensing,[37] the resonant linewidth of the plasmonic gratings (FWHM = 6.5 nm) is much smaller, as shown in the inset of Fig. 3(b). The photoelectric responses follow the optical properties exactly as shown in Fig. 3(d), where a responsivity peak at 914 nm with an FWHM of 6.69 nm was also observed. The normalized response bandwidth is 0.7%. Please note that the FWHMs of the peaks around 914 nm in Figs. 3(b)–3(d) are all overestimated due to the limited spectral resolution of the AOTF used, as shown in Figs. 2(g) and 2(h). To calibrate the devices more accurately, the measurement was also conducted in a wavelength range about 1550 nm, where a tunable laser source with a spectral resolution down to 1 pm was used. To do so, an oblique incidence angle of 45 deg was applied to shift the resonance from 914 to 1550 nm. As shown in Figs. 3(c) and 3(d), a peak at 1550 nm was observed with an FWHM of 2.65 and 2.6 nm in the absorption and photoelectric response spectra, respectively. The associated normalized response bandwidth is 0.17%, which is the smallest linewidth of PDs, to the best of our knowledge. Such an on-chip narrowband photodetection with low background in a broad wavelength range shows great potential in NDIR gas sensing, biofluorescent detection, and high-accuracy spectral sensing.[38–40] It is also interesting to see that such a wavelength-selective PD shows fast time-dependent offset current, indicating its capability for instant response, as shown in Fig. S1 in the Supplementary Material (S4).

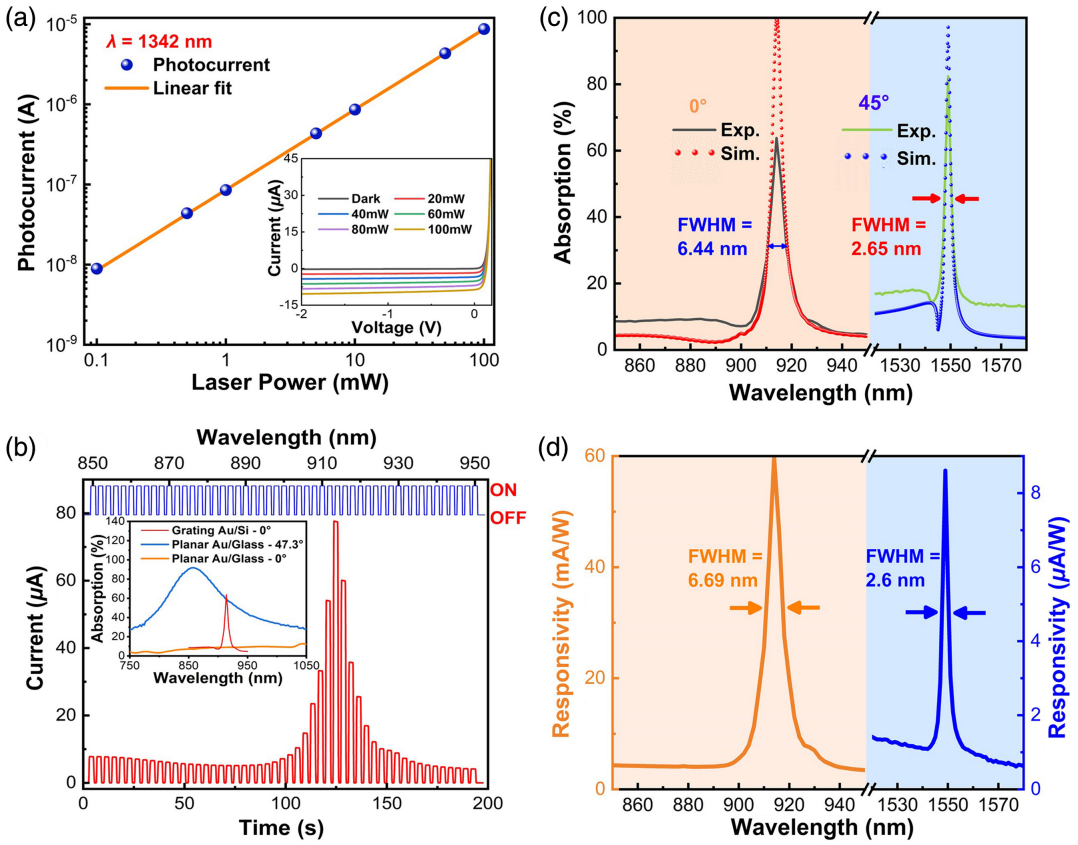

Fig. 3 Optoelectronic characterization of the proposed narrowband PDs. (a) Power-dependent photocurrent of the on-resonance device. The incident beam (launched by a 1342 nm laser) was fixed at an incident angle of 28.7 deg. The inset is the output $I-V$ curves measured under dark and light conditions. (b) Time-dependent photoelectric responses under different laser illuminations. The red line is the current, and the blue line is the driving signal. The inset shows the absorption spectra of Au/Si gratings, planar Au/glass at normal incidence, and a 45 deg incident angle for comparison. (c) Simulated and measured light absorption spectra of the associated Au/Si gratings at normal incidence and a 45 deg incident angle. (d) The responsivity of the device shown in (c).

3.4 On-Chip Optical Sensing with In Situ Photoelectric Conversion

Optical sensing techniques have unique advantages, including high accuracy, low time delay, and a spectral fingerprint. However, encoding a target signal to light and converting a light signal to an electric signal for easy readout are usually achieved in two separated components in conventional optical sensing platforms. As a result, such a bulky and complex system (e.g., spectrometer) is difficult to be incorporated in on-site sensing platforms. In contrast, the proposed sensor is fully self-contained, where plasmonic nanogratings not only enable strong optical field confinement and narrowband resonance for sensing but also provide high light absorption and *in situ* HE emission for photoelectric conversion.

First, we evaluate the bulk sensitivity of such a device, which is associated with refractive index variations in the whole environment around the device. In simulation, assuming a solution with uniform refractive index distribution filling the entire space surrounding the device, the calculated absorption spectra are shown in Fig. 4(a). Redshift of the resonance is observed when the refractive index increases. For $\Delta n = 0.003$, a redshift of $\Delta\lambda = 3$ nm is obtained, indicating a sensitivity of $S = 1000$ nm/RIU, as shown in Fig. 4(b), where the figure of merit (FoM $= S/\text{FWHM}$) reaches 220. Assuming a spectral resolution of 1 nm (1 pm), such a sensitivity gives a detection limit of 10^{-3} RIU (10^{-6} RIU) for a conventional wavelength-interrogation sensing mechanism based on spectrometers. Instead, a sensing signal can also be extracted by a simple amplitude interrogation, which excludes the requirements on an expensive spectrometer. As shown in Fig. 4(b), light absorption decreases from 73.6% to 22.6% at $\lambda = 1342$ nm for $\Delta n = 0.003$. A sensing experiment was conducted with a glucose solution. In general, increasing the concentration of glucose causes the increase of the refractive index of the solution and thus the redshift of the plasmonic resonance. At the initial stage, the device covered with deionized water has a resonance at $\lambda = 1344$ nm, which is slightly larger than the laser illumination wavelength (1342 nm). Therefore, a decrease of the output current was observed with the increasing of the glucose concentration, as shown in Fig. 4(c). For a refractive index variation $\Delta n = 0.0013$ from deionized water to a glucose solution (1%), the current changes 276.6 nA. Considering the noise level of 1.3 nA, the detection limit is ~0.0047% (i.e., 2.65×10^{-6} RIU) assuming a linear

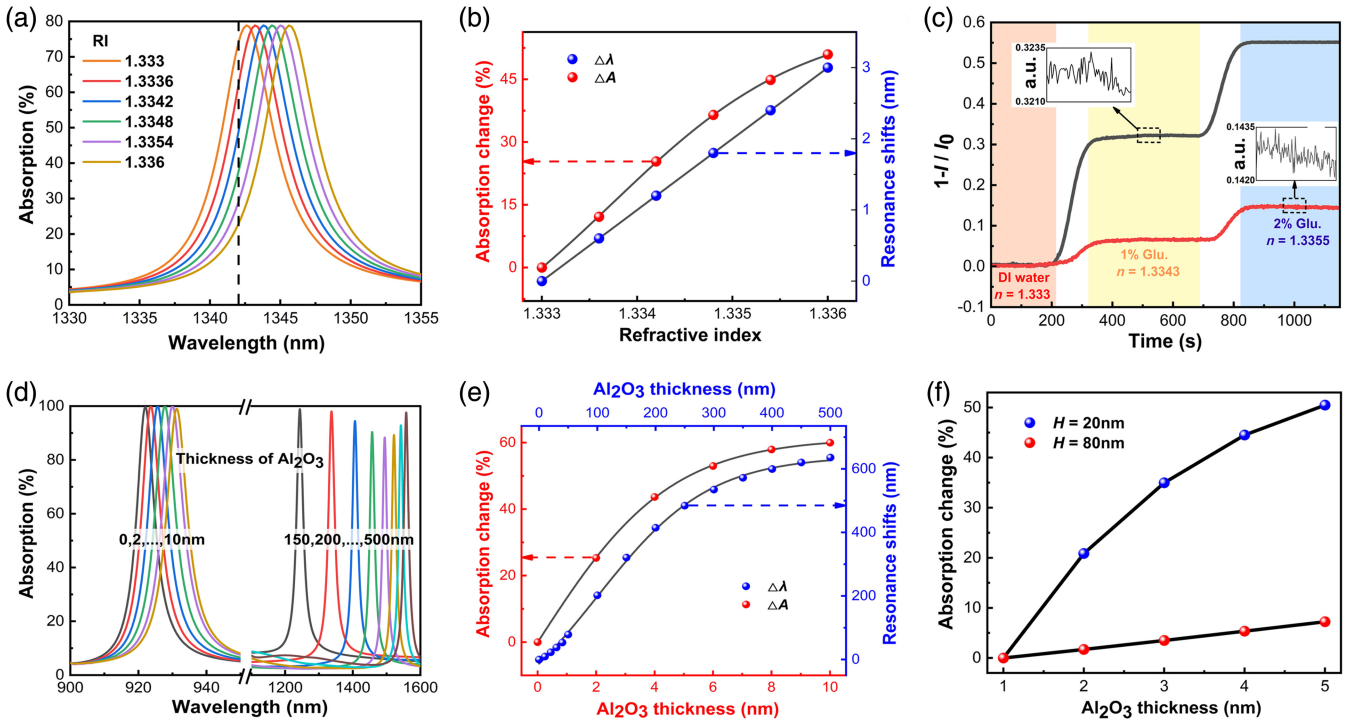

Fig. 4 Sensing performance of the narrowband plasmonic PD. (a) Calculated absorption spectra in the case of bulk sensing. $P = 900$ nm, $W = 477$ nm, $H = 28$ nm, and $t_{Au} = 60$ nm. (b) Resonance shift and absorption change of the results in (a) in the wavelength and amplitude interrogations, respectively. (c) Real-time output currents of two sensors with $H = 20$ nm (black line) and 80 nm (red line) in glucose solution sensing. (d) Calculated absorption spectra in the case of surface sensing. (e) Resonance shift and absorption change of the results in (c) in the wavelength and amplitude interrogations, respectively. (f) Calculated absorption change of two sensors with $H = 20$ nm (blue dots) and 80 nm (red dots) in surface sensing.

relation between the refractive index and the concentration. Glucose sensing experiments were also conducted on a same device with different laser sources (Supplementary Material S5), where it was found that the sensing signals of a laser with a narrower linewidth are larger than the one with a wider linewidth.

In contrast to bulk sensing, surface sensing is associated with the detection of thin films or bio/chemo interaction on the surface, where the refractive index variation only occurs in a region close to the sensor surface. Because the resonant field intensity of SPR usually decreases exponentially with a distance away from the surface, it is necessary to evaluate the surface sensing performance independently. Assuming a conformal thin film of Al_2O_3 is deposited on top of the plasmonic gratings, it induces a redshift of the calculated absorption spectrum, as shown in Fig. 4(d). For a 2 nm thick Al_2O_3, the resonance shift is 1.6 nm around $\lambda = 924$ nm and the absorption reduces from 71.3% to 45.9%, as shown in Fig. 4(e). By shifting the resonance to 1550 nm at an oblique incidence angle of 45 deg, $\Delta\lambda$ decreases to 0.42 nm for the same 2 nm film due to the further extension of the plasmonic field distribution. Therefore, the minimal detectable thickness of the Al_2O_3 film via the wavelength interrogation is less than 1.25 pm assuming a spectral resolution of 1 pm. In addition, the resonance shift becomes saturate when the film thickness increases beyond 500 nm because the surface mode becomes weak at the positions farther away from the sensor surface. Similarly, in surface sensing, a device with shallow gratings ($H = 20$ nm) has much larger absorption variation than the one with deep gratings ($H = 80$ nm).

To evaluate the actual biosensing performance of the proposed device, rabbit IgG detection was conducted. First, goat anti-rabbit IgG molecules in a concentration of 200 μg/mL were bonded onto the Au film at the sensor surface via covalent interaction. Then, rabbit IgG diluted with phosphate-buffered saline buffer in different concentrations was injected into the microfluidic in sequence. The interaction between rabbit IgG in the solution and the goat anti-rabbit IgG immobilized on the sensor surface was measured as a current signal in real time. As shown in Fig. 5, the current started to decrease right after the injection of the solutions with higher concentrations and became saturate after several minutes. It is because the capture of rabbit IgG in the solution caused an increase of the average refractive index in the region close to the sensor surface, and thus a redshift as in Fig. 4(a). The stable values of the current are ~1.87, 2.65, and 4.66 μA for 10, 50, and 100 μg/mL rabbit IgG, respectively. Considering the current noise of 20 nA during the measurement, the limit of detection (LOD) of rabbit IgG can be estimated to be 150 ng/mL, which is comparable to or better than most optical sensors in the literature. For example, H-shaped SPR fiber sensor showed an LOD of 3400 ng/mL for human IgG.[41] Decoration of $MoSe_2$ nanostructures on Au-coated optical fiber obtained an LOD of 330 ng/mL for goat-anti-rabbit IgG.[42] Immobilizing half-antibody fragments on an SPR fiber instead of antibody decoration reduced an

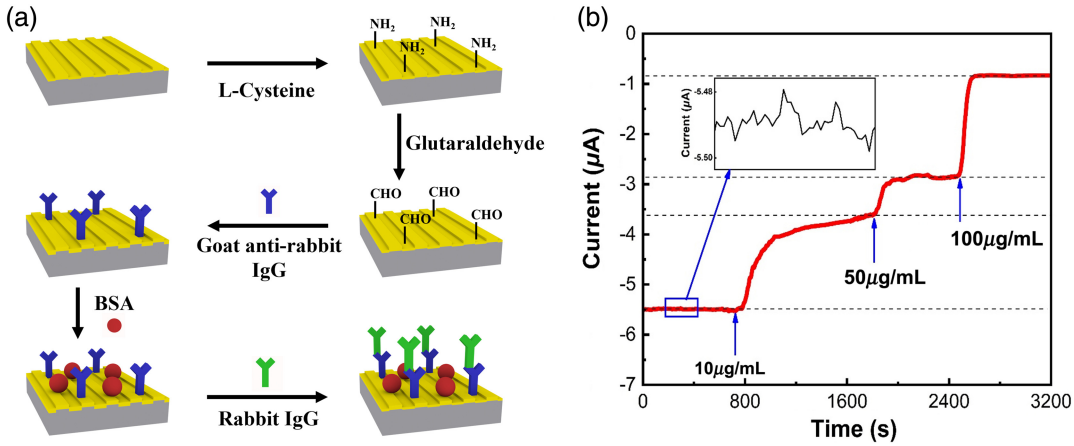

Fig. 5 Rabbit IgG detection experiment. (a) Schematic of plasmonic sensor surface modification and rabbit IgG detection process. (b) Real-time current output from the sensor with the rabbit IgG solution injection at three concentrations in sequence. The inset shows the noise level during the measurement.

LOD down to 100 ng/mL.[43] Please note that all these measurements relied on a precise spectroscopy instrument with a spectral resolution of 20 pm. In addition, a commercial SPR sensing instrument (Biacore X100) has an LOD of 312.5 ng/mL for rabbit IgG.[44] Therefore, the proposed self-contained plasmonic sensor based on a narrowband HE PD shows great advantages, with decent sensitivity, high integration, and low cost. Please note that this is the intrinsic sensing performance of the Au/Si gratings, and it could be significantly improved via advanced surface treatments and signal amplification techniques (e.g., graphene oxide and reduced graphene oxide decoration).[43–46]

4 Discussion

In this work, we demonstrated a narrowband PD (non-waveguide) with a record narrowband photoelectric response down to 2.6 nm at an operating wavelength of 1550 nm. Such a high wavelength selectivity in photodetection is expected to significantly improve the performance of sensing and spectroscopy. Continuous metal film covered shallow Si gratings were found to effectively suppress the radiative loss and thus support a narrow resonant linewidth with a low background signal in a broad wavelength range. Reducing light source divergence and linewidth was also suggested to realize narrowband photodetection. Benefiting from the HE based *in situ* photoelectric conversion in Au/Si Schottky junctions, self-contained on-chip optical sensing was achieved with an LOD of 150 ng/mL for rabbit IgG.

Disclosures

The authors declare no competing financial interests.

Code and Data Availability

The data that support the findings of this study are available from the corresponding author, Q.C., upon reasonable request.

Author Contributions

Q.C. and L.W. conceived the idea and designed the experiments. X.N., B.C., and H.W. fabricated the devices. X.N., W.L., H.H., Z.M., and N.T. contributed to photoelectric measurement and optical simulations. W.L., Z.L., J.P., and D.G. conducted the biosensing experiments. Q.C. and W.L. wrote the paper. All authors contributed to data analysis and scientific discussion.

Acknowledgments

We are grateful for financial support from the National Natural Science Foundation of China (Grant Nos. 62220106001 and 92050108), the Key Research and Development Program of Guangdong Province (Grant No. 2023B0101200009), the Guangdong Science and Technology Program International Cooperation Program (Grant No. 2021A0505030038), the Guangdong Basic and Applied Basic Research Foundation (Grant No. 2022B1515020069), and the Pearl River Talent Plan Program of Guangdong (Grant No. 2019QN01X120). We are also thankful for the technical support from Nano Fabrication Facility and Nano-X of SINANO, CAS.

References

1. R. Cheng, N. A. Jaeger, and L. Chrostowski, "Fully tailorable integrated-optic resonators based on chirped waveguide moiré gratings," *Optica* **7**, 647–657 (2020).
2. S. Nair, C. Escobedo, and R. G. Sabat, "Crossed surface relief gratings as nanoplasmonic biosensors," *ACS Sens.* **2**, 379–385 (2017).
3. M. Liang et al., "Development of an Au nanoclusters based activatable nanoprobe for NIR-II fluorescence imaging of gastric acid," *Biosens. Bioelectron.* **224**, 115062 (2023).
4. L. Kühner et al., "Nanoantenna-enhanced infrared spectroscopic chemical imaging," *ACS Sens.* **2**, 655–662 (2017).
5. Q. Chen et al., "Nanophotonic color routing," *Adv. Mater.* **33**, 2103815 (2021).
6. Q. Lin et al., "Filterless narrowband visible photodetectors," *Nat. Photonics* **9**, 687–694 (2015).
7. Y. Fang et al., "Highly narrowband perovskite single-crystal photodetectors enabled by surface-charge recombination," *Nat. Photonics* **9**, 679–686 (2015).
8. A. Armin et al., "Narrowband light detection via internal quantum efficiency manipulation of organic photodiodes," *Nat. Commun.* **6**, 6343 (2015).
9. W. Wang et al., "Highly narrowband photomultiplication type organic photodetectors," *Nano Lett.* **17**, 1995–2002 (2017).

10. J. Li et al., "Self-trapped state enabled filterless narrowband photodetections in 2D layered perovskite single crystals," *Nat. Commun.* **10**, 806 (2019).
11. L. Wang et al., "Highly sensitive narrowband Si photodetector with peak response at around 1060 nm," *IEEE Trans. Electron Devices* **67**, 3211–3214 (2020).
12. W. Ho et al., "Narrow-band metal-oxide-semiconductor photodetector," *Appl. Phys. Lett.* **94**(6), 061114 (2009).
13. S. Murtaza et al., "Resonant-cavity enhanced (RCE) separate absorption and multiplication (SAM) avalanche photodetector (APD)," *IEEE Photonics Technol. Lett.* **7**, 1486–1488 (1995).
14. X. Nie et al., "Strongly polarized quantum well infrared photodetector with metallic cavity for narrowband wavelength selective detection," *Appl. Phys. Lett.* **116**, 161107 (2020).
15. X. Tang et al., "Plasmon resonance enhanced colloidal HgSe quantum dot filterless narrowband photodetectors for mid-wave infrared," *J. Mater. Chem. C* **5**, 362–369 (2017).
16. H. Monshat, L. Liu, and M. Lu, "A narrowband photo-thermoelectric detector using photonic crystal," *Adv. Opt. Mater.* **7**, 1801248 (2019).
17. X. Tan et al., "Non-dispersive infrared multi-gas sensing via nanoantenna integrated narrowband detectors," *Nat. Commun.* **11**, 5245 (2020).
18. A. Solanki et al., "Harnessing the interplay between photonic resonances and carrier extraction for narrowband germanium nanowire photodetectors spanning the visible to infrared," *ACS Photonics* **5**, 520–527 (2018).
19. Q. Chen et al., "Ultra-broadband spatial light modulation with dual-resonance coupled epsilon-near-zero materials," *Nano Res.* **14**, 2673–2680 (2021).
20. L. Wen et al., "Broad-band spatial light modulation with dual epsilon-near-zero modes," *Opto-Electron. Adv.* **5**, 200093 (2022).
21. A. Sobhani et al., "Narrowband photodetection in the near-infrared with a plasmon-induced hot electron device," *Nat. Commun.* **4**, 1643 (2013).
22. M. Tanzid et al., "Combining plasmonic hot carrier generation with free carrier absorption for high-performance near-infrared silicon-based photodetection," *ACS Photonics* **5**(9), 3472–3477 (2018).
23. L. Wen et al., "Multiband and ultrahigh figure-of-merit nanoplasmonic sensing with direct electrical readout in Au-Si nanojunctions," *ACS Nano* **13**, 6963–6972 (2019).
24. H. Yan et al., "Wideband-tunable on-chip microwave photonic filter with ultrahigh-Q U-bend-Mach–Zehnder-interferometer-coupled microring resonators," *Laser Photonics Rev.* **17**, 2300347 (2023).
25. L. Huang et al., "Pushing the limit of high-Q mode of a single dielectric nanocavity," *Adv. Photonics* **3**, 016004 (2021).
26. S. N. Zheng et al., "Microring resonator-assisted Fourier transform spectrometer with enhanced resolution and large bandwidth in single chip solution," *Nat. Commun.* **10**, 2349 (2019).
27. Z. Sun et al., "Plasmonic near-infrared photoconductor based on hot hole collection in the metal-semiconductor-metal junction," *Molecules* **27**, 6922 (2022).
28. Y. Dong et al., "CMOS-compatible broad-band hot carrier photodetection with Cu–silicon nanojunctions," *ACS Photonics* **9**, 3705–3711 (2022).
29. L. Wen et al., "Enhanced photoelectric and photothermal responses on silicon platform by plasmonic absorber and Omni-Schottky junction," *Laser Photonics Rev.* **11**, 1700059 (2017).
30. Z. Qi et al., "Au nanoparticle-decorated silicon pyramids for plasmon-enhanced hot electron near-infrared photodetection," *Nanotechnology* **28**, 275202 (2017).
31. L. Wen et al., "Hot electron harvesting via photoelectric ejection and photothermal heat relaxation in hotspots-enriched plasmonic/photonic disordered nanocomposites," *ACS Photonics* **5**, 581–591 (2018).
32. C. Zhang et al., "Recent progress and future opportunities for hot carrier photodetectors: from ultraviolet to infrared bands," *Laser Photonics Rev.* **16**, 2100741 (2022).
33. C. Zhang et al., "Plasmonic nanoneedle arrays with enhanced hot electron photodetection for near-IR imaging," *Adv. Funct. Mater.* **33**, 2304368 (2023).
34. B. Gao et al., "Nanoscale refractive index sensors with high figures of merit via optical slot antennas," *ACS Nano* **13**, 9131–9138 (2019).
35. J. Wang et al., "Broadband Tamm plasmon-enhanced planar hot-electron photodetector," *Nanoscale* **12**, 23945–23952 (2020).
36. Z. Wang et al., "Narrowband thermal emission realized through the coupling of cavity and Tamm plasmon resonances," *ACS Photonics* **5**, 2446–2452 (2018).
37. L.-H. Jin, S.-M. Li, and Y.-H. Cho, "Enhanced detection sensitivity of pegylated CdSe/ZnS quantum dots-based prostate cancer biomarkers by surface plasmon-coupled emission," *Biosen. Bioelectron.* **33**, 284–287 (2012).
38. L. Wen et al., "On-chip ultrasensitive and rapid hydrogen sensing based on plasmon-induced hot electron–molecule interaction," *Light Sci. Appl.* **12**, 76 (2023)
39. Q. Chen et al., "On-chip readout plasmonic mid-IR gas sensor," *Opto-Electron. Adv.* **3**, 190040 (2020).
40. Q. Zheng et al., "On-chip near-infrared spectral sensing with minimal plasmon-modulated channels," *Laser Photonics Rev.* **17**, 2300475 (2023).
41. Y. Huang et al., "Compact surface plasmon resonance IgG sensor based on H-shaped optical fiber," *Biosensors* **12**, 141 (2022).
42. K. Liu et al., "$MoSe_2$-Au based sensitivity enhanced optical fiber surface plasmon resonance biosensor for detection of goat-anti-rabbit IgG," *IEEE Access* **8**, 660–668 (2020).
43. Z. Mai et al., "A disposable fiber optic SPR probe for immunoassay," *Biosens. Bioelectron.* **144**, 111621 (2019).
44. W.-S. Jiang et al., "Reduced graphene oxide-based optical sensor for detecting specific protein," *Sens. Actuators B: Chem.* **249**, 142–148 (2017).
45. J. Zhang et al., "A protein A modified Au-graphene oxide composite as an enhanced sensing platform for SPR-based immunoassay," *Analyst* **138**, 7175 (2013).
46. B. Wang et al., "An optical fiber immunosensor with a low detection limit based on plasmon coupling enhancement," *J Lightwave Technol.* **38**, 3781–3788 (2020).

Long Wen is a professor at the Institute of Nanophotonics at Jinan University. His research interests center on the applications of plasmonics to infrared light detection, modulation, biosensing, and multifunctional nanodevices. Currently, he is particularly interested in the integration of nanophotonics with various applications-specific platforms, such as CMOS image sensor, semiconductor devices, and microfluidics for developing more compact optoelectronic devices and systems.

Dan Gao is an associate professor in Tsinghua International Graduate School at Shenzhen, Tsinghua University. Her research focuses on the development of novel methods based on microfluidics combined with mass spectrometry and spectroscopic techniques for drug analysis, novel organic synthesis and biosensors. She received her PhD from Beijing University of Chemical Technology, China.

Qin Chen is a professor at the Institute of Nanophotonics, Jinan University, China. He directs a micro/nano-optoelectronic device group. His research interests include nanophotonics, photodetection, optical sensing, micro-spectroscopy, etc. He has developed sub-ppm MIS junction hydrogen sensors, infrared enhanced CMOS image sensor, on-chip spectral sensor, etc. He received his PhD in microelectronics and solid sold electronics from the Institute of Semiconductors, Chinese Academy of Sciences, in 2006.

Biographies of the other authors are not available.